JACS
JOURNAL OF THE AMERICAN CHEMICAL SOCIETY
Article
pubs.acs.org/JACS

Uncovering the Role of Oxygen Atom Transfer in Ru-Based Catalytic Water Oxidation

Dooshaye Moonshiram,[†,‡] Yuliana Pineda-Galvan,[†] Darren Erdman,[†] Mark Palenik,[§] Ruifa Zong,[∥] Randolph Thummel,[∥] and Yulia Pushkar*[,†]

[†]Department of Physics and Astronomy, Purdue University, 525 Northwestern Avenue, West Lafayette, Indiana 47907, United States
[‡]Chemical Sciences and Engineering Division, Argonne National Laboratory, 9700 S. Cass Avenue, Lemont, Illinois 60439, United States
[§]Code 6189, Chemistry Division, Naval Research Laboratory, 4555 Overlook Avenue SW, Washington, DC 20375, United States
[∥]Department of Chemistry, University of Houston, Houston, Texas 77204-5003, United States

Supporting Information

ABSTRACT: The realization of artificial photosynthesis carries the promise of cheap and abundant energy, however, significant advances in the rational design of water oxidation catalysts are required. Detailed information on the structure of the catalyst under reaction conditions and mechanisms of O−O bond formation should be obtained. Here, we used a combination of electron paramagnetic resonance (EPR), stopped flow freeze quench on a millisecond−second time scale, X-ray absorption (XAS), resonance Raman (RR) spectroscopy, and density functional theory (DFT) to follow the dynamics of the Ru-based single site catalyst, $[Ru^{II}(NPM)(4\text{-pic})_2(H_2O)]^{2+}$ (NPM = 4-*t*-butyl-2,6-di(1′,8′-naphthyrid-2′-yl)-pyridine, pic = 4-picoline), under the water oxidation conditions. We report a unique EPR signal with g-tensor, $g_x = 2.30$, $g_y = 2.18$, and $g_z = 1.83$ which allowed us to observe fast dynamics of oxygen atom transfer from the Ru^{IV}═O oxo species to the uncoordinated nitrogen of the NPM ligand. In few seconds, the NPM ligand modification results in $[Ru^{III}(NPM\text{-}NO)(4\text{-pic})_2(H_2O)]^{3+}$ and $[Ru^{III}(NPM\text{-}NO,NO)(4\text{-pic})_2]^{3+}$ complexes. A proposed $[Ru^{V}(NPM)(4\text{-pic})_2$═O$]^{3+}$ intermediate was not detected under the tested conditions. We demonstrate that while the proximal base might be beneficial in O−O bond formation via nucleophilic water attack on an oxo species as shown by DFT, the noncoordinating nitrogen is impractical as a base in water oxidation catalysts due to its facile conversion to the N−O group. This study opens new horizons for understanding the real structure of Ru catalysts under water oxidation conditions and points toward the need to further investigate the role of the N−O ligand in promoting water oxidation catalysis.

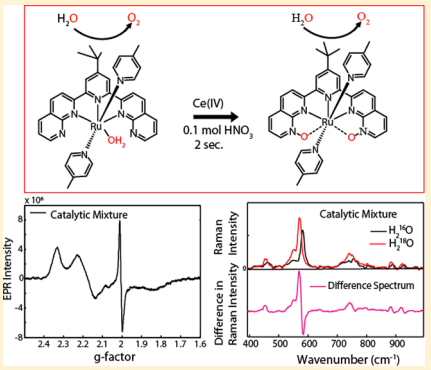

1. INTRODUCTION

Our society excels in producing electricity using alternative energy sources such as the sun and wind. However, without efficient energy storage, these intermittent sources will find only limited applications. The direct conversion of visible light to chemical energy by a synthetic device made of inorganic, organic, or hybrid materials is an attractive method for harvesting sunlight in the form of a fuel.[1−7] Mimicking the water oxidation reaction that occurs during natural photosynthesis in a man-made device will allow for such a conversion.[8−10] However, this process requires efficient catalysts, which can be incorporated into a molecular assembly, into other microscopic structures, or immobilized onto an electrode surface.[11−14] A detailed mechanistic knowledge of the catalytic action is required for the design of active and robust water oxidation catalysts (WOCs). In spite of emerging design principles, there remains a lack of general understanding about the structure−activity/stability relationship in water oxidation. Encouraging results have been obtained in recent years in finding more WOCs including those utilizing earth abundant elements; however, mechanistic insights into their action remain limited.[5,15]

For a fundamental understanding of the mechanism of WOCs, Ru based molecular complexes remain the most attractive due to their stability as homogeneous catalysts and the large number of available ligands for rational catalysts' designs. The majority of di-Ru[16−18] and mono-Ru[19−30] complexes utilize neutral polypyridine based ligands and water as a direct ligand to Ru.[22−26,31−34] Catalyst activation occurs via proton coupled electron transfer (PCET) and metal-oxo species are considered to be the key intermediates responsible for reactivity with water and O−O bond formation. Mechanistic analysis with spectroscopic identification of reactive intermediates is available for blue dimer (BD),[35−40] where the formation of the Ru^{IV},Ru^{V} intermediate was

Received: August 11, 2016
Published: November 1, 2016

DOI: 10.1021/jacs.6b08409
J. Am. Chem. Soc. 2016, 138, 15605−15616

confirmed by X-ray spectroscopy(XAS),[38] and the spin density of the radicaloid Ru^{V}=O fragment was mapped experimentally by electron paramagnetic resonance (EPR).[37] We have further demonstrated through EPR and XAS that, for a monomeric $[Ru^{II}(bpy)(tpy)H_2O]^{2+}$ catalyst, 95% of the Ru complex in the catalytic steady state exists in the form of $[Ru^{IV}(bpy)(tpy)=O]^{2+}$.[41] Spectroscopic measurements have also helped to clarify the role that chloride and iodide ligands to Ru play in controlling the water oxidation catalysis.[41,42] During these studies, we gained the first insights in how quickly the Ru ligand environment can be modified under catalytic conditions. For instance, we demonstrated that the Ru−I bond in the $[Ru^{II}(bpy)(tpy)I]^{+}$ catalyst is cleaved within a few seconds after the addition of an oxidant, followed by the formation of the reactive $[Ru^{IV}(bpy)(tpy)=O]^{2+}$ species.[42] Additionally, oxidation of two nitrogens in the 2,2′:6′,2″:6″,2‴-quaterpyridine (qpy) ligand, with formation of N−O groups, was reported to result in an active WOC.[43]

Activation of the Ru-based complexes toward catalysis via PCET and the O−O bond formation step require the removal of protons; thus, some catalysts' ligands were designed to facilitate proton abstraction.[44] Here, we spectroscopically analyze the single-site water oxidation catalyst $[Ru^{II}(NPM)(4\text{-pic})_2(OH_2)]^{2+}$ (**1**) (NPM = 4-*t*-butyl-2,6-di(1′,8′-naphthyrid-2′-yl)pyridine, pic = 4-picoline)[45,31,46] (Scheme 1). Interestingly, this catalyst has two noncoordinating nitrogen centers on the NPM ligand, which were suggested to work as an internal base and facilitate proton removal. This particular complex has been proposed to make the O−O bond via water nucleophilic attack on either the highly oxidized Ru^{V}=O intermediate (at acidic pH), or the less oxidized Ru^{IV}=O (neutral pH) intermediate. Spectroscopic signatures of the presumed $[Ru^{IV}-OO]^{2+}$ intermediate characterized through resonance Raman (RR) and mass spectrometry have been taken as evidence for O−O bond formation from the Ru^{IV}=O state at neutral pH.[31,46] These interesting claims mandate an in-depth spectroscopic analysis.

Here, a combination of EPR, together with ms-s freeze quench sample preparation, XAS, RR and DFT analysis are used to follow the catalyst's evolution during water oxidation (Scheme 1). We found that the $[Ru^{IV}(NPM)(4\text{-pic})_2=O]^{2+}$ intermediate created under water oxidizing conditions undergoes facile, as fast as 2 s., oxygen atom transfer to the uncoordinated nitrogen of the NPM ligand. The resulting $[Ru^{III}(NPM\text{-}NO)(4\text{-pic})_2(H_2O)]^{3+}$ and $[Ru^{III}(NPM\text{-}NO,NO)(4\text{-pic})_2]^{3+}$ complexes are characterized by unique EPR signals and specific ^{18}O isotope sensitive modes in RR. An earlier assignment to a $[Ru^{IV}-OO]^{2+}$ intermediate[31] has thus been revised. Additionally, we show that the use of uncoordinated nitrogen centers in a catalyst's design as an expected base should be treated with caution, as they can be quickly modified by facile oxygen atom transfer from Ru^{IV}=O state to form N−O bonds. This, previously unaccounted for, reactivity can be potentially responsible for some other spectroscopic misinterpretations by UV−vis spectroscopy, such as reports on rates of Ru^{V}=O formation and its reactivity with water in $[Ru(tpy)(bpm)(H_2O)]^{2+}$, where tpy =2,2′:6′,2″-terpyridine and bpm =2,2′-bipyrimidine, which contains two noncoordinating nitrogen ligands.[47] Overall results show the critical importance of understanding the ligand structure around the metal center under catalytic conditions.

Scheme 1. Proposed Catalyst Evolution for $[Ru^{II}(NPM)(4\text{-pic})_2(H_2O)]^{2+}$ Shown in This Work

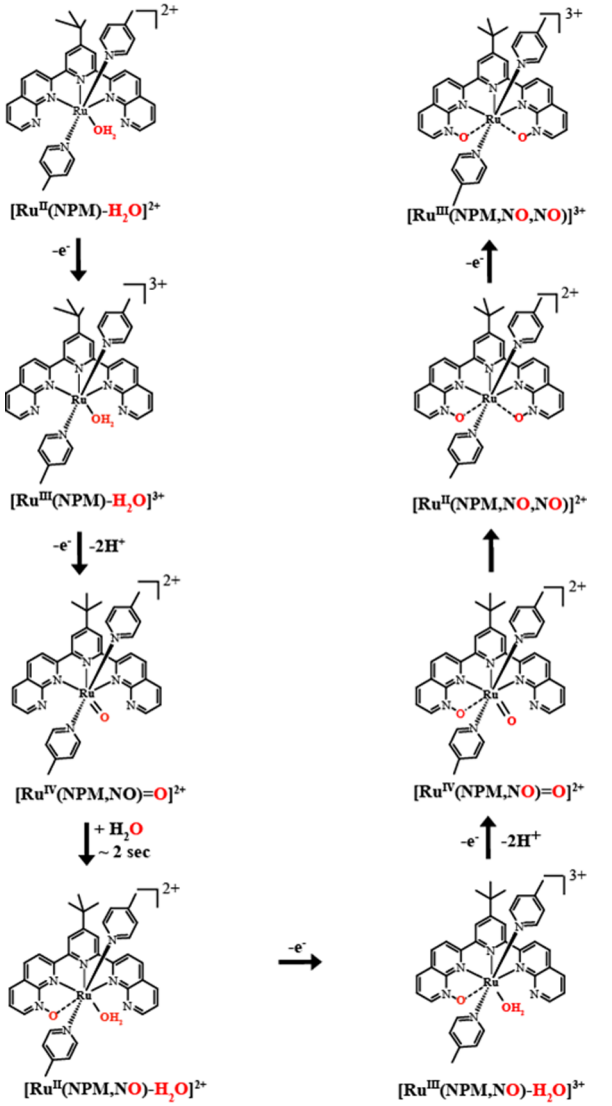

2. MATERIALS AND METHODS

2.1. Sample Preparation. $[Ru^{II}(NPM)(4\text{-pic})_2(OH_2)]^{2+}$ and $[Ru^{II}(tpy)(4\text{-pic})_2(H_2O)]^{2+}$ were synthesized according to a reported procedure.[45] Ultrapure (Type 1) water (resistivity 18.2 MΩ cm at 25 °C, TOC 4 μg/L) was used for solutions. All samples were prepared in 0.1 M HNO_3 acid, pH 1.0 (catalog no. 225711 from Sigma-Aldrich). Oxidant solutions were prepared fresh daily by dissolving $Ce(NH_4)_2(NO_3)_6 \cdot 4H_2O$ in 0.1 M HNO_3. A Cary 300 Bio UV−vis spectrophotometer (Varian, Inc.) was used to monitor UV−visible spectra (5×10^{-5} M concentration) (Figure S1). All solutions for preparation of EPR samples were bubbled with argon to displace dissolved oxygen. Freezing of the EPR samples is accomplished by immersing EPR tube into liquid nitrogen precooled ethanol and takes 1−2 s. Thawing of the EPR samples takes about 30 s.

2.2. Stopped-Flow Freeze-Quench Spectroscopy. A stopped-flow UV−vis spectrometer (Applied Photophysics Ltd.) with a dead time of 0.5 ms was used to follow the reactions. The changes in the absorbance were monitored starting at 1 ms after Ce^{IV} addition. Cuvettes with path lengths of 2 mm and 10 mm were used to study changes in the absorbance of concentrated, $0.25-0.1 \times 10^{-3}$ M, and more dilute samples, $0.5-1 \times 10^{-4}$ M, respectively. To prepare samples for XAS and EPR, fast freeze-quenching of reaction mixtures was performed by using an SFM 20 Stopped-Flow System (Bio-Logic

DOI: 10.1021/jacs.6b08409
J. Am. Chem. Soc. 2016, 138, 15605−15616

Science Instruments). The apparatus is equipped with an umbilical connector with a built-in ejection nozzle at the end of the aging loop which sprays the aged reaction mixtures into precooled liquid pentane at −120 °C. The samples were collected from liquid pentane with EPR collection kits. In order to ensure that intermediates do not react with pentane at −120 °C, the samples were also collected by spraying reaction mixtures into liquid nitrogen. All the intermediates were observed using pentane (−120 C°) as well as liquid nitrogen as cryogens. Liquid nitrogen provides slower freezing rate and should not be used for monitoring short (less than 2 s) reactions.

2.3. EPR. Low-temperature X-band EPR spectra were recorded on a Bruker EMX X-band spectrometer equipped with an X-Band CW microwave bridge. The sample temperature was maintained at 20 K by use of an Air Products LTR liquid helium cryostat. Spectrometer conditions with microwave frequency 9.47 GHz; field modulation amplitude 10 G at 100 kHz and 31.7 mW microwave power were used.

2.4. Resonance Raman. Resonance Raman spectra were measured using a Horiba XploRA system, which contains a laser, microscope, and CCD camera. The built in 532 nm laser was used to excite all samples, in combination with an 1800 gr./mm grating, at a power of 20 mW. The samples were kept frozen at 77 K using a Linkam BCS196 cryostage combined with a liquid nitrogen pump. In addition, the sample and window space of the cryostage were continuously purged with nitrogen. For ^{18}O labeling studies, 1 mM of $[Ru^{II}(NPM)(4\text{-pic})_2(OH_2)]^{2+}$ was prepared in a solution of 90% $H_2{}^{18}O$ and 10% acetonitrile and incubated for a period of at least 24 h, to ensure that ^{18}O labeling was complete. To generate oxidized samples, 1, 2, 3, or 20 equiv. Ce^{IV} in 1 M HNO_3 were added to 36 μL of 1 mM solution of Ru complex. All scans were recorded with 5 s exposure and no laser-induced damage was observed in consecutive scans.

2.5. XANES and EXAFS. X-ray absorption spectra were collected at the Advanced Photon Source (APS) at Argonne National Laboratory on bending magnet beamline 20 at incident photon electron energy 23 keV and average current 100 mA. The radiation was monochromatized by a Si(110) crystal monochromator. The intensity of the X-rays was monitored by three ion chambers (I_0, I_1 and I_2) filled with 70% nitrogen and 30% argon, which were placed before the sample (I_0) and after the sample (I_1 and I_2). A Ru metal foil was placed between the I_1 and I_2, and its absorption was recorded with each scan for energy calibration. The Ru XAS energy was calibrated by the first maxima in the second derivative of the ruthenium metal XANES spectrum (22117 eV).

Plastic (Lexan) EXAFS sample holders (inner dimensions of 12 mm × 3 mm × 3 mm) filled with frozen solutions were inserted into the precooled (20 K) cryostat. The samples were kept at 20 K in a He atmosphere at ambient pressure. The data were recorded as fluorescence excitation spectra using a 13-element energy-resolving detector. In order to reduce a risk of sample damage by X-ray radiation, 80% flux was used in the defocused mode (beam size 1 × 10 mm), and no damage was observed scan after scan to any samples. The samples were also protected from the X-ray beam during spectrometer movements by a shutter synchronized with the scan program. No more than 5 scans were taken at each sample position.

EXAFS data were analyzed using the Athena software package.[48] All data were background-corrected, normalized, and deglitched(if necessary), then converted to wave vector space (k-space) and weighted by k^3. k-space data were truncated near zero crossings before Fourier transformation. The Artemis software package was used for curve fitting. The peaks were either isolated and fitted separately or grouped together and fitted. Curve fitting was done using ab initio calculated phases and amplitudes from the FEFF8 code.[49] These amplitudes and phases were used in the EXAFS equation (eq 1):

$$\chi(k) = {S_0}^2 \sum_j \frac{N_j}{kR_j{}^2} f_{\mathrm{eff}_j}(\pi, k, R_j)\, e^{-2\sigma_j{}^2 k^2}\, e^{-2R_j/\lambda_j(k)} \sin(2kR_j + \phi_{ij}(k)) \quad (1)$$

where N_j is number of atoms in the jth shell, R_j is mean distance between absorbing atom and atoms in the jth shell, and f_{eff_j} is calculated amplitude function. The Debye−Waller term $e^{-2\sigma 2k^2}$ accounts for damping caused by thermal disorder. The $e^{-2R_j/\lambda_j(k)}$ term reflects losses caused by inelastic scattering. $\lambda_j(k)$ is the electron mean free path, φ_{ij} is the calculated phase function, and ${S_0}^2$ is the amplitude reduction factor.

This equation was used to fit the experimental Fourier isolated data (q-space) and Fourier transformed data (R-space) using N, R, E_0 and σ^2 as variable parameters. ${S_0}^2$ was set to be equal to 1. The quality of fit was evaluated by the R-factor (less than 2% denotes a good fit[50]), and the reduced χ^2 value was used to compare fits as more backscatters are included. A smaller χ^2 value implies a better fit.

2.6. DFT Calculations. The DFT calculations were performed with Gaussian09 using the B3LYP exchange-correlation (XC) functional. The 6-31G* basis was set for all organic atoms (C, O, N, H), and the all electron DGDZVP basis was set for the Ru atom. The CPCM polarizable conductor model was used to model water solvation and two explicit water molecules were included. The value of the reference potential (NHE) was assigned value to 4.44 V and the solvation free energy of a proton to −11.64 V. These results are shown in Tables 2, 3, S1, and S2.

Transition state calculations were performed using the synchronic transit-guided quasi-Newton (STQN) method. The STQN method, which locates transition states along a pathway between two points in configuration space, requires optimized reactants and products with equivalent sets of nuclei. The reactant and product geometries used in the STQN calculation were optimized with one explicit water molecule and the proton released during O−O bond formation was included in the product.

3. RESULTS

3.1. Low Temperature EPR Spectroscopy. Figure 1 shows the results of the EPR analysis of $[Ru^{II}(NPM)(4\text{-pic})_2(H_2O)]^{2+}$ oxidized with increasing stoichiometric amounts of Ce^{IV} in 0.1 M HNO_3 and frozen within 30 s. The sample prepared upon addition of 1 equiv of Ce^{IV} shows an $S = 1/2$ EPR signal corresponding to the $[Ru^{III}(NPM)(4\text{-}$

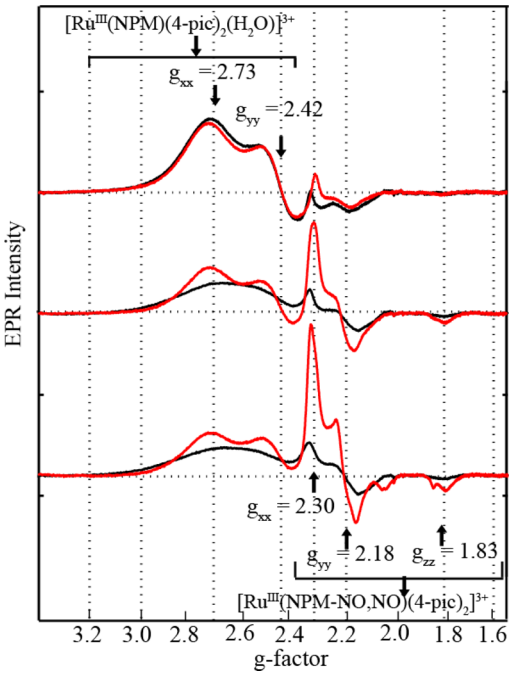

Figure 1. X-Band EPR (20 K) of 1 mM solutions of $[Ru^{II}(NPM)(4\text{-pic})_2(H_2O)]^{2+}$ in 0.1 M HNO_3 frozen within 30 s after addition of 1, 2, or 3 equiv of Ce^{IV} (black); the same samples melted for 1 min and refrozen for EPR analysis (red). A new EPR signal with g-tensor: g_x = 2.30, g_y = 2.18 and g_z = 1.83 is observed.

DOI: 10.1021/jacs.6b08409
J. Am. Chem. Soc. 2016, 138, 15605−15616

pic)$_2$(OH$_2$)]$^{3+}$ complex. Its g-tensor (g_{xx} = 2.73, g_{yy} = 2.42 while g_{zz} component was unresolved) and overall spectral shape is similar to that detected for other Ru^{III} (low spin, d^5) complexes with nitrogen and oxygen ligands.[41,51] EPR analysis of the solutions prepared by addition of 2 and 3 equiv of Ce^{IV} followed by rapid (30 s) freezing show that the samples still contain a mixture of the [Ru^{III}(NPM)(4-pic)$_2$(H$_2$O)]$^{3+}$; however, its EPR intensity is decreased. This indicates the presence of an EPR-silent species which accounts for the decreased intensity of the [Ru^{III}(NPM)(4-pic)$_2$(H$_2$O)]$^{3+}$ signal. The EPR-silent species accounting for the decrease in the EPR intensity can be [Ru^{IV}(NPM)(4-pic)$_2$=O]$^{2+}$ (S = 1) the product of the 2 electron oxidation of the initial complex. A new EPR signal with a less anisotropic g-tensor was also observed in samples prepared with 2 and 3 equiv of Ce^{IV}. Interestingly, quick 1 min melting and refreezing of the samples results in the increase of the signal with g-tensor g_{xx} = 2.30, g_{yy} = 2.18 and g_{zz} = 1.83. The signal of the [Ru^{III}(NPM)(4-pic)$_2$(H$_2$O)]$^{3+}$, on the other hand, does not increase by a significant amount. The sample prepared by addition of 3 equiv of Ce^{IV} demonstrates the largest intensity of this new EPR signal. We explain the observed increase in the total EPR intensity by the conversion of the EPR undetectable 2e$^-$ oxidation product ([Ru^{IV}(NPM)(4-pic)$_2$=O]$^{2+}$) into the EPR active (S = 1/2) 3e$^-$ oxidation intermediate. Intriguingly, the new EPR signal is already present in samples produced by addition of 2 and 3 equiv of Ce^{IV}, indicating that it is rapidly formed.

In order to follow fast formation of the new EPR signal, we prepared freeze-quenched samples by oxidation of the [Ru^{II}(NPM)(4-pic)$_2$(H$_2$O)]$^{2+}$ complex with 20 equiv of Ce^{IV}, representing catalytic conditions with millisecond−second time resolution. Interestingly, the new EPR signal appears as early as 2 s after mixing, Figure 2, reaches its maximum at about 40−60 s, and remains detectable at later times (up to 15 min), while the intensity of [Ru^{III}(NPM)(4-pic)$_2$(H$_2$O)]$^{3+}$ diminishes quickly, Figure 2. It is also important to note that while samples created by addition of 1−3 equiv. Ce^{IV} (Figure 1) do not show signal in g-factor range 2.1−1.8, freeze-quenched samples do have a singlet signal at about g ∼ 2.0. This signal has the maximum intensity at 60 s (green line, Figure 2), disappears upon melting(data not shown), and does not display a clear g_{xx} component expected for Ru^V or Ru^{99,101} hyperfine splittings. It is therefore difficult to exclude small contributions (below 5%) of Ru^V with confidence. However, as explained further in the discussion section (section 4.3), [Ru^{II}(NPM)(4-pic)$_2$(H$_2$O)]$^{2+}$ is less suitable for analysis of the Ru^V state due to facile modification of the ligand environment, which happens as fast as 2 s.

The following arguments can be put forward to assign the new S = 1/2 signal (g_{xx} = 2.30, g_{yy} = 2.18, and g_{zz} = 1.83). We note that addition of as little as 2 equiv of Ce^{IV} (Figure 1) results in the formation of an intermediate with a new EPR signal. This intermediate likely arises from the [Ru^{IV}(NPM)(4-pic)$_2$=O]$^{2+}$ state. It is possible that [Ru^{IV}(NPM)(4-pic)$_2$=O]$^{2+}$ directly reacts with water generating [Ru^{II}(NPM)(4-pic)$_2$OOH]$^{+}$, which is later oxidized to form [Ru^{III}(NPM)(4-pic)$_2$OOH]$^{2+}$ (new S = 1/2 EPR signal) upon melting. To verify this, EPR of the very similar (but lacking two noncoordinating nitrogen centers) catalyst [Ru^{II}(tpy)(4-pic)$_2$(H$_2$O)]$^{2+}$, was recorded (Figure 3). Indeed, titration of the [Ru^{II}(tpy)(4-pic)$_2$(H$_2$O)]$^{2+}$ catalyst shows absence of new EPR signals except for that of [Ru^{III}(tpy)(4-pic)$_2$(H$_2$O)]$^{3+}$. Oxidation with 2 equiv or more of Ce^{IV} simply results in the EPR silent [Ru^{IV}(tpy)(4-pic)$_2$=O]$^{2+}$ species, as shown by the decrease of the EPR signal upon melting. This suggests that the signal with g-tensor, g_x = 2.30, g_y = 2.18, and g_z = 1.83, is related to the presence of extra nitrogens. Thus, we assign this EPR signal to [Ru^{III}(NPM-NO)(4-pic)$_2$(H$_2$O)]$^{3+}$, which is formed from [Ru^{IV}(NPM)(4-pic)$_2$=O]$^{2+}$ by oxygen atom

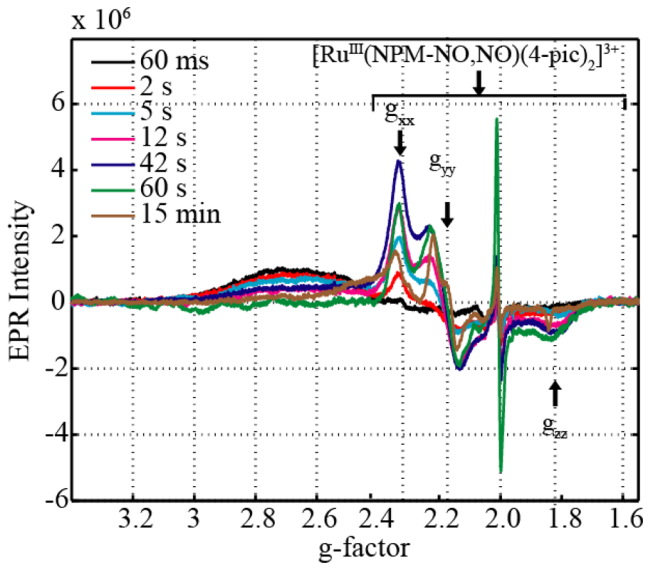

Figure 2. X-Band EPR (20 K) of 0.5 mM solutions of [Ru^{II}(NPM)(4-pic)$_2$(H$_2$O)]$^{2+}$ in 0.1 M HNO$_3$ mixed with 20 equiv of Ce^{IV} and frozen at indicated time intervals using the freeze-quench setup.

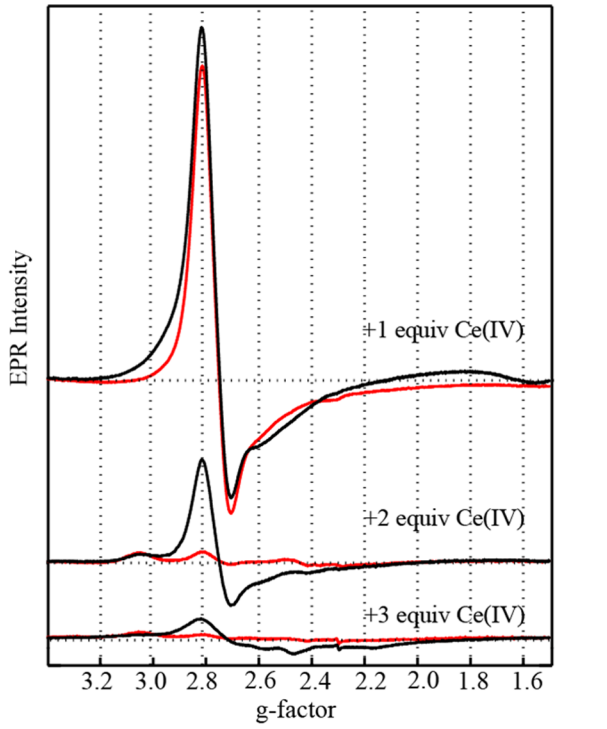

Figure 3. X-Band EPR (20 K) of 1 mM solutions of [Ru^{II}(tpy)(4-pic)$_2$(H$_2$O)]$^{2+}$ in 0.1 M HNO$_3$, frozen within 30 s after addition of 1, 2, or 3 equiv of Ce^{IV} (black); same samples melted for 1 min and refrozen for EPR analysis (red).

DOI: 10.1021/jacs.6b08409
J. Am. Chem. Soc. 2016, 138, 15605−15616

transfer to the noncoordinated nitrogen of the NPM ligand, making $[Ru^{II}(NPM\text{-}NO)(4\text{-}pic)_2(H_2O)]^{2+}$ and its later $1e^-$ oxidation by other $[Ru^{IV}(NPM)(4\text{-}pic)_2{=}O]^{2+}$ molecule.

The $[Ru^{III}(NPM\text{-}NO)(4\text{-}pic)_2(H_2O)]^{3+}$ intermediate has the characteristic g-tensor and smaller EPR line widths. Note that the long-term survival of the Ru^{III} species (up to 15 min in melted samples) in a highly oxidizing environment (after adding 20 equv of Ce^{IV}) indicates that this Ru^{III} species is harder to oxidize than the analogous $Ru^{III}{-}H_2O$ species. This argument makes us think that the final product corresponds to $[Ru^{III}(NPM\text{-}NO,NO)(4\text{-}pic)_2]$ which has Ru coordinated equatorially by two nitrogens of NPM and two oxygens of newly generated NO groups. This intermediate does not have water coordinated to Ru^{III} and thus cannot undergo redox levering via PCET. Further elaborations of this hypothesis can be found in the DFT, Raman, and Discussion sections.

To test the effect of the polypyridine−N-O ligand on the g-tensor of the Ru complexes, we synthesized $[Ru(bpy)_2(bpy\text{-}NO)]^{3+}$ (bpy-NO = bipyridine-*N*-oxide) analogue, $S = 1/2$, see Supporting Information for the synthesis description. We demonstrated that presence of the bpy-*N*-oxide ligand coordinated to Ru results in a low anisotropy g-tensor ($g_{xx} \sim 2.3$, $g_{yy} \sim 2.2$, $g_{zz} = 1.85$) due to larger delocalization of the spin density onto the organic ligand, which can be described by the following resonances: $Ru^{III}(ligand\text{-}NO) = Ru^{IV}(ligand\text{-}NO^{\bullet})$ (Figure S2).

3.2. X-ray Absorption Spectroscopy. The results of Ru K-edge XANES and EXAFS analysis of the $[Ru^{II}(NPM)(4\text{-}pic)_2(H_2O)]^{2+}$ under water oxidation catalysis are shown in Figure 4. Table S3 shows results of the EXAFS fits of the initial $[Ru^{II}(NPM)(4\text{-}pic)_2(H_2O)]^{2+}$ compound. Figure S3 compares experimental EXAFS and EXAFS FEFF profiles obtained by simulation of the multiple scattering paths from the crystal coordinates of the $[Ru^{II}(NPM)(4\text{-}pic)_2(H_2O)]^{2+}$.[45] EXAFS derived structural parameters are in very good agreement with the reported XRD structure and show Ru−N interactions at 1.94 and 2.11 Å as well as Ru−O at 2.22 Å in the first coordination sphere of the Ru center, Tables S3 and 1.

Oxidation with 1 equiv of Ce^{IV} results in the $[Ru^{III}(NPM)(4\text{-}pic)_2(H_2O)]^{3+}$ oxidized species with the absorption edge (XANES) shifted toward higher energy. This result is in agreement with the EPR results (Figure 1) showing that addition of 1 equiv of Ce^{IV} results in mostly Ru^{III} sample. EXAFS shows changes in the first and second coordination sphere with oxidation, Figure 4B. The first peak becomes more intense, showing less heterogeneity in the first coordination sphere of Ru. The Ru−C ligand peaks also appear at slightly shorter distances, Tables 1 and S4. We investigated the hypothesis of the Ru^{III} disproportionation with formation of $Ru^{IV}{=}O$ species by introducing the Ru−O vector at 1.8 Å in EXAFS fits. Addition of 50% or 25% of $Ru^{IV}{=}O$ species did not result in fit improvement (data not shown). We concluded that EXAFS analysis does not indicate any significant formation of $Ru^{IV}{=}O$ in samples obtained with 1 equiv of Ce^{IV}.

Addition of 20 equiv. Ce^{IV} followed by quick freezing results in an oxidized species with assigned oxidation state + IV as shown from the XANES comparison with the RuO_2 reference, Figure 4A. By EPR, this sample demonstrates an admixture of the Ru^{III} species of possibly $[Ru^{III}(NPM\text{-}NO,NO)(4\text{-}pic)_2]^{3+}$ nature. However, the integrated intensity of this EPR is quite low (10−20% of the total Ru species). We expect that the majority of the Ru species in the sample frozen within 30 s after addition of 20 equiv of Ce^{IV} exists as the Ru^{IV} species, which

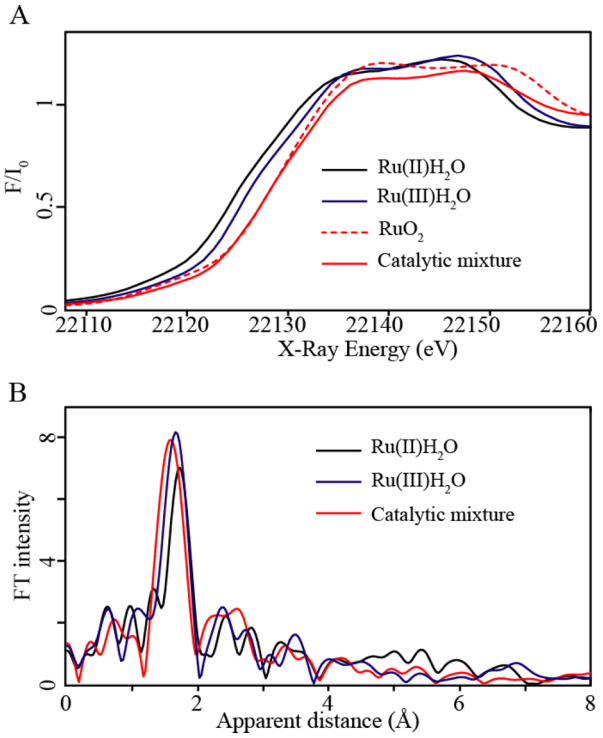

Figure 4. Comparison of the spectroscopic characteristic (20 K) of $[Ru^{II}(NPM)(4\text{-}pic)_2(H_2O)]^{2+}$, $[Ru^{III}(NPM)(4\text{-}pic)_2(H_2O)]^{3+}$ and catalytic mixture generated by the addition of 20 equiv of Ce^{IV} and frozen within 30 s. (A) Normalized Ru K-edge XANES including reference compound RuO_2. (B) Fourier transforms of k^3- weighted Ru EXAFS (for associated fits see Tables 1 and S3−S5, Figures S3 and S4).

can be both $[Ru^{IV}(NPM)(4\text{-}pic)_2{=}O]^{2+}$ and $[Ru^{IV}(NPM\text{-}NO)(4\text{-}pic)_2{=}O]^{2+}$. In EXAFS, the first and second peaks shift to lower distances, Figure 4B, Tables 1 and S4. All EXAFS fits show improvement of the overall fit quality upon addition of a Ru−O distance at 1.8 Å, in agreement with the XANES data showing predominant presence of a Ru^{IV} species. Introduction of the Ru−O vector at 2.5 Å additionally results in fit improvements. This likely relates to the formation of $[Ru^{III}(NPM\text{-}NO,NO)(4\text{-}pic)_2]^{3+}$, which has a significantly modified ligand environment, see Table S2.

3.3. Resonance Raman. Resonance Raman (RR) was recorded using 532 nm excitation at cryogenic conditions on initial $[Ru^{II}(NPM)(4\text{-}pic)_2(H_2O)]^{2+}$ sample and reaction mixtures oxidized with Ce^{IV}. RR spectrum of initial compound is overall similar to earlier reported.[30] Here we focus on the 400−1000 cm^{-1} range for analysis, as it contains the Ru−O vibrations. The RR spectrum for $[Ru^{II}(NPM)(4\text{-}pic)_2(H_2{}^{18}O)]^{2+}$ shows no change after 24 h. incubation of the $[Ru^{II}(NPM)(4\text{-}pic)_2(H_2O)](ClO_4)_2$ salt in 100% $H_2{}^{18}O$, Figure S5. This result is in agreement with earlier reports for the blue dimer where $Ru{-}OH_2$ vibration was not detectable in RR.[37,50]

Oxidation with 1 equiv of Ce^{IV} results in sample color change from blue/purple to yellow. Previous studies[31] have shown that both Ru^{III} and Ru^{IV} intermediates have a decreased (by a factor of ~2−3) absorption at 532 nm in comparison with $[Ru^{II}(NPM)(4\text{-}pic)_2(H_2O)]^{2+}$. The intensity of the RR signal recorded in similar conditions shows little change, indicating sufficient Raman enhancement in spite of the lower absorbance for the oxidized species prepared with 1 equiv of Ce^{IV}. The RR

DOI: 10.1021/jacs.6b08409
J. Am. Chem. Soc. 2016, 138, 15605−15616

Table 1. Structural Parameters from Selected EXAFS Fits[a] (for More Details, See Tables S3–S5)

sample	shell	R, Å	σ^2 ($\times 10^{-3}$)
$Ru^{II}(NPM)(4\text{-pic})_2(H_2O)]^{2+}$	Ru–N, 1	1.94	1.0[b]
	Ru–N, 4	2.11	1.0[b]
R-factor = 0.0001	Ru–O, 1	2.22	1.0[b]
reduced χ^2 = 88.6	Ru–C, 4	2.97	1.2[b]
fit no. 10, Table S3	Ru–C, 6	3.14	1.2[b]
	Ru–N, 2	3.31	1.2[b]
bond distances from XRD:[c]			
Ru–N: 1.92, 2.09,2.09, 2.10, 2.10			
Ru–O: 2.14			
$Ru^{III}(NPM)(4\text{-pic})_2(H_2O)]^{3+}$	Ru–N, 4	2.09	0.9[b]
	Ru–N, 2	2.22	0.9[b]
R-factor = 0.0005	Ru–C, 4	2.97	0.2[b]
reduced χ^2 = 1636	Ru–C, 6	3.13	0.2[b]
fit no. 5, Table S4	Ru–N, 2	3.28	0.2[b]
$[Ru^{II}(NPM)(4\text{-pic})_2(H_2O)]^{2+}$ oxidized with 20 equiv of Ce^{IV} and frozen within 30 s	Ru–O, 1	1.73	1.4
	Ru–N, 5	2.09	4.1[b]
R-factor = 0.0001	Ru–O, 2	2.58	4.1[b]
reduced χ^2 = 213.3	Ru–C, 8	3.02	7.0[b]
fit no. 10, Table S5	Ru–C, 2	3.53	7.0[b]

[a]Fits were done in q-space. R is the Ru–backscatter distance. σ^2 is Debye–Waller factor. R-factor and reduced χ^2 are the goodness-of-fit parameters (see the Supporting Information, XAS/EXAFS section). S_0^2 = 1.0 was used in all fits. [b]σ^2 was set to be the same for close by shells. [c]XRD data are taken from ref 45.

spectra of the oxidized $[Ru^{III}(NPM)(4\text{-pic})_2(H_2O)]^{3+}$ intermediate is similar to that of $[Ru^{II}(NPM)(4\text{-pic})_2(H_2O)]^{2+}$. No major peak shifts are detected for the $[Ru^{III}(NPM)(4\text{-pic})_2(H_2{}^{18}O)]^{3+}$ intermediate, Figure S6. Similarly, addition of 2 and 3 equiv of Ce^{IV} in $H_2{}^{16}O$ or $H_2{}^{18}O$ result in no distinct changes or appearance of new bands, Figure S7. $Ru^{IV}{=}O$ vibration is expected at ~780 cm^{-1} and should undergo about 35–40 cm^{-1} shift when labeled with ^{18}O, as shown from DFT predicted value, see Table S6.[52] Lack of the $Ru^{IV}{=}O$ vibration in RR can be explained by its weak resonant enhancement at 532 nm.

Addition of 4 or 20 equiv of Ce^{IV} to $[Ru^{II}(NPM)(4\text{-pic})_2(H_2O)]^{2+}$ results in a color change from blue/purple to red-brown in agreement with that reported previously,[31] with a UV–visible absorption of 512 nm (Figure S8). Significant changes in the Raman spectrum (Figure 5) are observed consisting of peak shifts, the appearance of new Raman bands as well as changes in relative peak intensities. Some of these changes can be explained by the different resonance enhancement of the ligand modes in the intermediate absorbing at 512 nm while others reflect a ligand modification. New Raman bands appearing below ~1050 cm^{-1} suggest changes in the Ru coordination environment. The $H_2{}^{18}O$ labeled oxidized species show multiple Raman shifts as compared to the $H_2{}^{16}O$ labeled derivative; for instance the band, at 461 cm^{-1} shifts to 455 cm^{-1} (−6 cm^{-1}), 582 cm^{-1}, shifts to 574 cm^{-1} (−8 cm^{-1}) and that at 774 cm^{-1} shifts to 755 cm-1 (−19 cm^{-1}) upon ^{18}O labeling. In addition, the two Raman bands at ~888 and 926 cm^{-1} demonstrate a small shift of 3 cm^{-1}. All these changes become even more pronounced in samples generated by addition of 20 equiv of Ce^{IV} (Figure 6), likely due to a higher amount of the

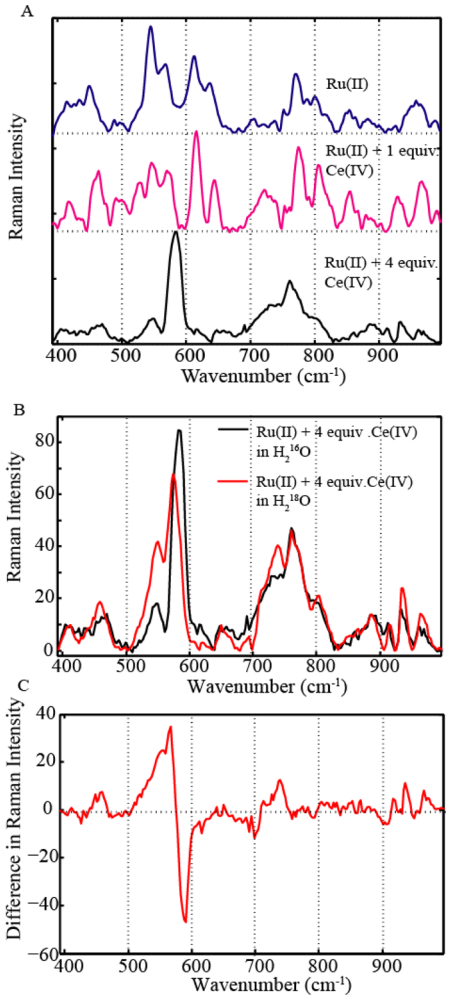

Figure 5. RR (77 K) of $[Ru^{II}(NPM)(4\text{-pic})_2(H_2O)]^{2+}$ (1 mM, 0.1 M HNO_3) with excitation at 532 nm (A) in regular water and oxidized with 1 and 4 equiv of Ce^{IV} and (B) oxidized with 4 equiv of Ce^{IV} in ^{16}O and ^{18}O enriched water. (C) ^{18}O–^{16}O difference spectra for samples oxidized with 4 equiv of Ce^{IV}.

product absorbing at 512 nm. Note that no changes in the Raman spectra were observed for 1 min melted and refrozen samples produced with 2 or 3 equiv of Ce^{IV}. On the other hand, upon melting the oxidized species produced with 4 or 20 equiv of Ce^{IV}, the Raman band at 574 cm^{-1} increases in intensity showing the dynamics of product formation (Figure S9A). In summary, the RR results mirror very well those reported previously,[31] while our analysis of difference spectra allows better identification of bands affected by isotope shifts. The only difference observed for oxidized samples with Ce^{IV} is the predominant character of the 574 cm^{-1} band. On the other hand, the samples obtained through bulk electrolysis (BE) (pH = 6, 1150 mV relative to NHE) in previous studies[31] showed a predominant feature at 547 cm^{-1}. In order to verify that the shift of 547 cm^{-1} is not due to a pH effect, we repeated the RR measurements after a pH jump and observed no change in the spectrum (data not shown). We also noted that the BE sample was produced under relatively mild redox potentials. For instance, after addition of 20 equiv of a weaker oxidant, sodium periodate, the RR spectrum with a Raman band of 547 cm^{-1} was observed (Figure S10).

While we have very similar RR results, our interpretation differs significantly from that shown previously.[31] We note that

DOI: 10.1021/jacs.6b08409
J. Am. Chem. Soc. 2016, 138, 15605–15616

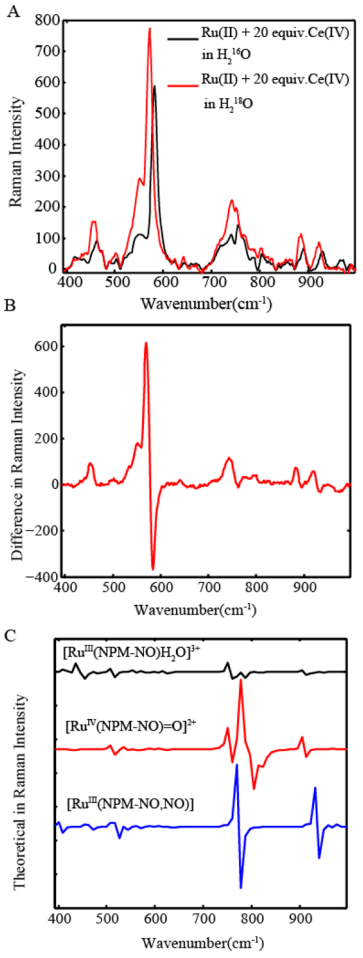

Figure 6. (A) RR (77K) of $[Ru^{II}(NPM)(4\text{-pic})_2(H_2O)]^{2+}$ (1 mM, 0.1 M HNO_3) with excitation at 532 nm oxidized with 20 equiv of Ce^{IV} in $H_2{}^{16}O$ and $H_2{}^{18}O$, melted for 1 min and measured refrozen. (B) $^{18}O-{}^{16}O$ difference spectrum. (C) Difference Raman spectra from DFT of three selected models with NPM-NO ligands, Table S6. Note that DFT computed regular Raman (not RR) gives information on peak positions and isotope shifts but not on peak intensities.

there are more isotope sensitive bands than the peroxide models can account for, Table S6. At the same time, the observed isotope shifts are too small in magnitude to correspond to Ru−O or O−O bonds which are respectively predicted to have ∼15−20 cm^{-1} and ∼50−80 cm^{-1} isotope shifts. The interpretation derived from EPR analysis, implying oxidation of the noncoordinating nitrogens, fits much better the RR results. In addition, DFT calculations for the models with the NPM-NO and NPM-NO,NO ligands all indicate that the bands in the range of 500−600, ∼760, and 900−940 cm^{-1} will be present and undergo only small 5−10 cm^{-1} isotope shifts (Figure 6C). This is due to the significant coupling of the vibrations in the Ru−O−N fragment with breathing modes of the NPM ligand. We believe that the $[Ru^{III}(NPM\text{-}NO,NO)]^{3+}$ intermediate is the most likely candidate due to its stability under oxidizing conditions and its paramagnetic S = 1/2 character; however, presence of several intermediates in the mixture cannot be excluded.

3.4. DFT Results. DFT has been used to aid in the interpretation of spectroscopic results. We have performed calculations for the standard, currently accepted in the literature mechanism of water oxidation via water nucleophilic attack on Ru-oxo species, Figure 7 (black squares). Results of DFT calculations for intermediates expected to occur in the oxidation process are presented in Tables 2 and S1, and Figure 7.

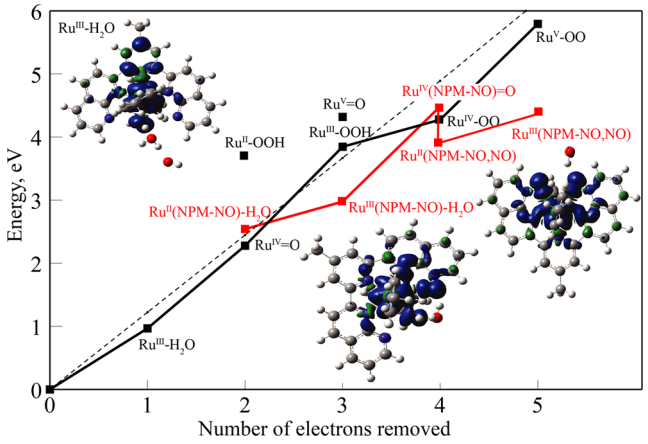

Figure 7. DFT (UB3LYP/DGDZVP) derived Latimer−Frost diagram for oxidation of $[Ru^{II}(NPM)(4\text{-pic})_2(H_2O)]^{2+}$ (structure shown in the top left corner) under standard conditions (pH = 0). Main path (black squares) corresponds to the mechanisms with water nucleophilic attack on Ru-oxo species while red squares show the ligand modification pathway. Note that formal "Ru^{IV}−OO" and "Ru^{V}−OO" states are $[Ru^{III}-O_2{}^{\bullet-}]$ and $[Ru^{III}-O_2]$, correspondingly. Dashed line corresponds to the 1.23 eV water oxidation potential at pH = 0. Insets show the spin density of $[Ru^{III}(NPM)(4\text{-pic})_2(H_2O)]^{3+}$, $[Ru^{III}(NPM\text{-}NO)(4\text{-pic})_2(H_2O)]^{3+}$, and $[Ru^{III}(NPM\text{-}NO,NO)(4\text{-pic})_2]^{3+}$ paramagnetic intermediates.

Table 2. Experimental and DFT Derived Redox Potentials at pH = 0 for $[Ru^{II}(NPM)(4\text{-pic})_2(H_2O)]^{2+}$

redox couple	exp/V[a]	cal/V[b]	|Δ|/V
$[Ru^{III}-OH_2]^{3+}/[Ru^{II}-OH_2]^{2+}$	0.98 (0.96)	0.97	0.03 (0.20)
$[Ru^{IV}=O]^{2+}/[Ru^{III}-OH_2]^{3+}$	1.33 (1.57)	1.13	0.20 (0.08)
$[Ru^{V}=O]^{3+}/[Ru^{IV}=O]^{2+}$	1.69 (1.66)	2.24	0.55 (0.27)

[a]Values in brackets are DFT computed redox potentials from refs 31 and 46. [b]DFT computed in this work, Table S1.

The selection of DFT parameters has been verified by comparison of the redox potential of the known Ru^{II}/Ru^{III} and Ru^{III}/Ru^{IV} couples[31,46] at pH = 0, Table 2. As seen in Table 2, computed results for Ru^{II}/Ru^{III} and Ru^{III}/Ru^{IV} couples redox potentials agree with experimental measurements within the commonly accepted ∼200 mV range for DFT precision.[53] They also agree with previously reported DFT derived redox potentials for these couples,[31] Table 2. Large deviation is apparent for the $[Ru^{V}=O]^{3+}/[Ru^{IV}=O]^{2+}$ couple. This is likely due to significant ambiguity in determining the redox potential for this transition experimentally. The discrepancy in this case is similar to that reported for the Ru^{IV}/Ru^{V} couple of the $[Ru^{II}(bpy)(tpy)H_2O]^{2+}$ catalyst.[41] Surprisingly, prior DFT analysis of the redox potential for $[Ru^{V}(NPM)(4\text{-pic})_2{=}O]^{3+}$ formation provided 1.66 V[31] which is in disagreement with the 2.24 V obtained, Table 2. We have not detected $[Ru^{V}(NPM)(4\text{-pic})_2{=}O]^{3+}$ $S = 1/2$ signal in this study, but have to note that the range of interest has several overlapping EPR signals which prevents detection of any small signals (5% or below). In order to test the facility of $[Ru^{V}(NPM)(4\text{-pic})_2{=}O]^{3+}$ species in reactions with water with O−O bond formation, we carried

DOI: 10.1021/jacs.6b08409
J. Am. Chem. Soc. 2016, 138, 15605−15616

Table 3. Theoretical Analysis of Energetic of the Oxygen Atom Transfer Intermediates in $[Ru^{II}(NPM)(4\text{-pic})_2(H_2O)]^{2+}$

elemental steps	$\Delta G°$/eV	$E°$/V
oxygen atom transfer		
Ru^{IV}═O; $2H_2O$═Ru^{II}(NPM-NO)−H_2O; H_2O	0.27	
Ru^{IV}(NPM-NO)═O; H_2O═Ru^{II}(NPM-NO,NO) + H_2O	−0.50	
oxidation		
Ru^{III}(NPM-NO)−H_2O; H_2O + $1e^-$ = Ru^{II}(NPM-NO)−H_2O; H_2O	−4.87	0.43
Ru^{IV}(NPM-NO)═O; H_2O + $1e^-$ + $2H^+$═Ru^{III}(NPM-NO)−H_2O; H_2O	−29.07	1.35
Ru^{III}(NPM-NO,NO) + $1e^-$ = Ru^{II}(NPM-NO,NO)	−4.88	0.44
Ru^{V}(NPM-NO)═O; H_2O + $1e^-$ = Ru^{IV}(NPM-NO)═O; H_2O	−6.53	2.08
Ru^{IV}(NPM-NO,NO) + $1e^-$ = Ru^{III}(NPM-NO,NO)	−6.38	1.94
O−O bond formation		
Ru^{IV}(NPM-NO)═O; H_2O═Ru^{IV} − OO; H_2O, TS = 1.89 eV	−0.13	
Ru^{III}(NPM-NO,NO);H_2O═Ru^{III}−H_2O + O_2	−0.35	

out a transition state analysis. Our transition state optimizations found the Ru^{V}═O to Ru^{III}−OOH Gibbs free energy activation barrier to be 0.38 eV. We included a single explicit water molecule in this calculation, which is split into H^+ and OH^-. By performing various geometry optimizations, we found that the lowest energy pathway for the proton in our model was to bond with a nearby nitrogen atom. Although the reaction pathway of the real system likely differs due to interactions with additional solvent molecules, this provided a convenient boundary for a STQN calculation.

Spectroscopic characteristics such as spin density distributions (Figure 7) and Raman modes (Table S6, Figure 6C) have been calculated for the products of O−O bond formation in the standard pathway. In the standard pathway, DFT optimization of the formal states "Ru^{IV}−OO" and "Ru^{V}−OO" resulted in $[Ru^{III}-O_2^{\bullet-}]$ and $[Ru^{III}-O_2]$ states, as can be inferred from bond distances and spin density distributions, see Table S1 and Figure 7.

Our spectroscopic results indicate that ligand modification occurred as fast as 2 s after initiation of catalysis. Thus, we also used DFT to calculate Gibbs free energies to show that oxygen atom transfer is energetically favorable between the Ru^{IV}═O species and noncoordinating nitrogen, Table 3. $\Delta G°$ for conversion of the $[Ru^{IV}(NPM)(4\text{-pic})_2$═$O]^{2+}$ to $[Ru^{II}(NPM\text{-}NO)(4\text{-pic})_2(H_2O)]^{2+}$ was estimated at about ∼0.3 eV. However, the $[Ru^{II}(NPM\text{-}NO)(4\text{-pic})_2(H_2O)]^{2+}$ product can be easily oxidized to $[Ru^{III}(NPM\text{-}NO)(4\text{-pic})_2(H_2O)]^{3+}$ at only ∼ +0.4 V (Table 3) thus shifting equilibrium. We think that the formed $[Ru^{II}(NPM\text{-}NO)(4\text{-pic})_2(H_2O)]^{2+}$ is quickly oxidized by $[Ru^{IV}(NPM)(4\text{-pic})_2$═$O]^{2+}$ or Ce^{IV} present in solution. Thus, formation of both $[Ru^{III}(NPM\text{-}NO)(4\text{-pic})_2(H_2O)]^{3+}$ and $[Ru^{III}(NPM)(4\text{-pic})_2(H_2O)]^{3+}$ is predicted from $[Ru^{IV}(NPM)(4\text{-pic})_2$═$O]^{2+}$, which is exactly observed in the experiment when both EPR signals are growing upon melting, Figure 1. DFT results show that spin density on Ru decreases from ∼0.91 for $[Ru^{III}(NPM)(4\text{-pic})_2(H_2O)]^{3+}$ to ∼0.84 for $[Ru^{III}(NPM\text{-}NO)(4\text{-pic})_2(H_2O)]^{3+}$, which is in a good agreement with a less anisotropic EPR g-tensor, due to larger delocalization of spin density on the ligands in $[Ru^{III}(NPM\text{-}NO)(4\text{-pic})_2(H_2O)]^{3+}$. To justify the presence of Ru^{III} species under strongly oxidizing Ce^{IV} conditions at pH = 1, we proposed formation of $[Ru^{III}(NPM\text{-}NO,NO)(4\text{-pic})_2]^{3+}$. The spin density for Ru in this structure is only ∼0.77 indicating even larger delocalization onto the ligand. Overall spin density distributions for these species are shown as insets in Figure 7. To obtain $[Ru^{III}(NPM\text{-}NO,NO)(4\text{-pic})_2]^{3+}$ product, $[Ru^{III}(NPM\text{-}NO)(4\text{-pic})_2(H_2O)]^{3+}$ is first oxidized via PCET to form $[Ru^{IV}(NPM\text{-}NO)(4\text{-pic})_2$═$O]^{2+}$ with estimated $E°$ = 1.35 V (Table 3, Figure 7, Scheme 1). $[Ru^{IV}(NPM\text{-}NO)(4\text{-pic})_2$═$O]^{2+}$ subsequently undergoes oxygen atom transfer to form $[Ru^{II}(NPM\text{-}NO,NO)(4\text{-pic})_2]^{2+}$. This process is predicted to be more facile ($\Delta G°$ = −0.5 eV) in comparison with the first step of O-transfer ($\Delta G°$ = 0.27 eV). Oxidation of $[Ru^{II}(NPM\text{-}NO,NO)(4\text{-pic})_2]^{2+}$ to $[Ru^{III}(NPM\text{-}NO,NO)(4\text{-pic})_2]^{3+}$ is predicted to take place at 0.44 V while the next oxidation step is significantly high in energy at about 1.9 V, Table 3. Thus, from an energetics standpoint, $[Ru^{III}(NPM\text{-}NO,NO)(4\text{-pic})_2]^{3+}$ appears to be a steady state product under strongly oxidizing conditions such as the presence of Ce^{IV} oxidant.

We also investigated whether a modified ligand with an N−O bond might be directly involved in O−O bond formation. The $[Ru^{IV}(NPM\text{-}NO)$═$O]^{2+}$ intermediate can be converted to the $[Ru^{IV}$−$OO]^{2+}$ peroxo species with small negative ΔG (−0.13 eV, Table 3, Figure 7), however, there appears to be a larger driving force for its conversion to $[Ru^{II}(NPM\text{-}NO,NO)]^{2+}$ ∼ −0.5 eV. We found the transition state for O−O bond formation in $[Ru^{IV}(NPM\text{-}NO)$═$O]^{2+}$ to be relatively high (∼1.9 eV), such that formation of $[Ru^{II}(NPM\text{-}NO,NO)]^{2+}$ appears to be more likely.

4. DISCUSSION

Here, we monitored water oxidation catalysis by the single site Ru-based catalyst $Ru^{II}(NPM)(4\text{-pic})_2(H_2O)]^{2+}$ using a combination of EPR, freeze quench stopped flow, UV−vis, X-ray absorption, and resonance Raman spectroscopic techniques. To simplify discussion, we first address the formation of various reactive Ru species, categorizing them by oxidation state of Ru center, then we discuss implications for the water oxidation mechanism and catalyst design.

4.1. Ru^{III} Species. Based on previous UV−vis analysis,[31] $[Ru^{III}(NPM)(4\text{-pic})_2(H_2O)]^{3+}$ complex was found to be unstable and therefore was generated via pulse radiolysis. However, here we generated $[Ru^{III}(NPM)(4\text{-pic})_2(H_2O)]^{3+}$ by oxidation with 1 equiv of Ce^{IV} in 0.1 M HNO_3 and observed its S = 1/2 EPR signal with g-tensor g_{xx} = 2.73, g_{yy} = 2.42 and unresolved g_{zz} component. This species is stable on a minute time scale (Figure 1). The EPR signal of the $[Ru^{III}(NPM)(4\text{-pic})_2(H_2O)]^{3+}$ was also recorded after oxidation with 1 equiv of $NaIO_4$ in 0.1 M HNO_3 (data not shown). DFT calculations show that disproportionation of this complex to Ru^{IV} and Ru^{II} species is unlikely at pH = 0, $\Delta G°$ = +0.42 eV and requires removal of two protons for which there is no driving force at acidic pH. $[Ru^{III}(tpy)(4\text{-pic})_2(H_2O)]^{3+}$ was studied for

DOI: 10.1021/jacs.6b08409
J. Am. Chem. Soc. 2016, 138, 15605−15616

comparison and its $S = 1/2$ EPR signal has close to cylindrical symmetry g-tensor with $g_{xx} \approx g_{yy} = 2.49$ and $g_{zz} = 1.54$. This signal disappeared with addition of 3 equiv of Ce^{IV} indicating full conversion to EPR silent Ru^{IV} species.

4.2. Ru^{IV} Species. $[Ru^{IV}(NPM)(4\text{-pic})_2{=}O]^{2+}$ can be generated by oxidation of $[Ru^{II}(NPM)(4\text{-pic})_2(H_2O)]^{2+}$ with two or more equiv of Ce^{IV}. This species is EPR silent, and loss of the $[Ru^{III}(NPM)(4\text{-pic})_2(H_2O)]^{3+}$ signal intensity in Ce^{IV} titration is associated with formation of $[Ru^{IV}(NPM)(4\text{-pic})_2{=}O]^{2+}$. Under catalytic conditions, immediately after addition of 20 equiv of Ce^{IV}, the majority of the Ru exists in oxidation state Ru^{IV}, see XANES results in Figure 4A. This result is in good agreement with XANES characterization of other single site Ru catalysts, $[Ru^{II}(bpy)(tpy)H_2O]^{2+}$ and $[Ru^{II}(bpy)(tpy)I]^{+}$, which shows that majority of Ru species in catalytic steady state are represented by the $Ru^{IV}{=}O$ species.[41,42] EXAFS fits point toward a $Ru^{IV}{=}O$ distance at 1.73 Å (Table 1) which is shorter when compared with 1.80 Å in $[Ru^{IV}(bpy)(tpy){=}O]^{2+}$.[41,42] DFT predicts $Ru^{IV}{=}O$ distance at 1.80 Å for $[Ru^{IV}(NPM)(4\text{-pic})_2{=}O]^{2+}$ and 1.77 Å for $[Ru^{IV}(NPM\text{-}NO)(4\text{-pic})_2{=}O]^{2+}$. It appears that $Ru^{IV}{=}O$ oscillation is not detectable with 532 nm excitation wavelength, likely due to its lack of resonance enhancement. The $Ru^{IV}{=}O$ species demonstrated reactivity in oxygen atom transfer and formed a Ru complex with modified ligand. This process was monitored by freeze quench and EPR ($S = 1/2$ signal with $g_{xx} = 2.30$, $g_{yy} = 2.18$, and $g_{zz} = 1.83$) and was shown to happen as quickly as 2 s after addition of Ce^{IV} oxidant. Addition of $NaIO_4$ oxidant also resulted in $Ru^{IV}{=}O$ intermediate followed by formation of Ru complex with modified ligand (EPR data not shown). Ru complexes with $Ru^{IV}{=}O$ fragment are known to be active in oxygen atom transfer;[54] however, this is the first time that its reactivity has been delineated under conditions of water oxidation and that its time course has been determined.

4.3. Ru^{V} Species. The requirement of the formation of the highly oxidized $Ru^{V}{=}O$ fragment as a prerequisite to O−O coupling step in single site Ru catalysts has dominated the earlier (2009−2013) literature. So far, the claimed rate limiting $[Ru^{V}(bpy)(tpy){=}O]^{3+}$[23,47,53,55−58] was not observed under any experimental conditions, and, according to DFT, it might be thermodynamically inaccessible (requires 2.13 V) via oxidation with Ce^{IV} (1.67 V at pH = 0).[41] The high oxidation potential of the $Ru^{IV}{=}O$ to $Ru^{V}{=}O$ transition in single site Ru catalysts with neutral polypyridine ligands cannot be offset by the effect of proton coupled electron transfer (PCET). A similarly high redox potential for Ru^{IV}/Ru^{V} couple was calculated here for $[Ru^{II}(NPM)(4\text{-pic})_2(H_2O)]^{2+}$, Table 2.

As explained in section 3.1, we attempted detection of $S = 1/2$ $[Ru^{V}(NPM)(4\text{-pic})_2{=}O]^{3+}$ by EPR, Figures 1 and 2. Polyansky et al.[31] suggested through UV−vis analysis and Pourbaix diagram that this species exist in close to 1:1 ratio with $[Ru^{IV}(NPM)(4\text{-pic})_2{=}O]^{2+}$ due to the close redox potentials of the Ru^{III}/Ru^{IV} and Ru^{IV}/Ru^{V} transitions. Such high content of the $[Ru^{V}(NPM)(4\text{-pic})_2{=}O]^{3+}$ is ruled out by our EPR measurements, Figures 1 and 2. However, as explained above, the $[Ru^{II}(NPM)(4\text{-pic})_2(H_2O)]^{2+}$ catalysts appears to be less suitable for analysis of the $Ru^{V}{=}O$ species due to facile modification of its ligand. According to DFT calculations, the Ru^{V} state is slightly easier to achieve in complexes with a modified ligand environment: 2.08 eV (Table 3) versus 2.24 eV (Table 2). Thus, even if Ru^{V} would be detected in this system, verification of its exact ligand environment would be required.

4.4. $[Ru^{IV}{-}OO]^{2+}$ Species Reinterpreted. Previously reported bulk electrolysis at potentials below 1.4 V, but above the potential of Ru^{III}/Ru^{IV} and Ru^{II}/Ru^{IV} couples, resulted in red colored solutions containing peroxide product $[Ru^{IV}{-}OO]^{2+}$.[31] We observed similar color changes for reaction mixtures generated with Ce^{IV}. The effect is most pronounced with the addition of four or more equiv of Ce^{IV}. Mass spectroscopy of BE samples indicated mass of $[Ru(NPM)(4\text{-pic})_2O,O]^{2+}$ which was presented as a confirmation of the peroxide product $[Ru^{IV}{-}OO]^{2+}$.[31] However, the increase of its mass by 16 also fits the description of the $[Ru^{IV}(NPM\text{-}NO)(4\text{-pic})_2{=}O]^{2+}$ and $[Ru^{II}(NPM\text{-}NO,NO)(4\text{-pic})_2]^{2+}$ which are products with modified ligands. A second confirmation of the peroxide product $[Ru^{IV}{-}OO]^{2+}$ was presented by Raman spectroscopy; however, only one band at 547 cm^{-1} and its isotope shift of −12 cm^{-1} with ^{18}O was discussed. The fact that O−O vibration was not reported and isotope shift of 12 cm^{-1} is low for a Ru−O bond (expected to have ∼20 cm^{-1} isotope shift) makes the assignment questionable. If the Ru complex follows the water oxidation pathway with $Ru^{V}{=}O$ or $Ru^{IV}{=}O$ directly reacting with water with formation of the $Ru^{III}{-}OOH$ and $Ru^{IV}{-}OO$ species, only two bands with ^{18}O isotope shift − Ru−O and O−O should be observed and the shifts ought to be significant, Table S6. Previous studies[31] reported shift of the Raman bands at 930−920 cm^{-1} and 800−760 cm^{-1} without interpretation. In our RR experiments, we found more vibrations that change with ^{18}O and the shifts are relatively modest which makes RR results compatible with ligand modification. In the modified ligand, the Ru−O mode is coupled to the ligand breathing modes making isotope shifts smaller, Figure 6C.

Moreover, a new EPR signal in which the g-tensor is consistent with modification of the Ru ligand, was detected from BE samples provided by Polyansky, Figure S11.

Redox behavior of the BE product[31] showed a first redox transition at about 0.5 V at pH = 1 with pH dependence of pK_a value close to 3.5. This transition has characteristics which match very well predicted DFT for the following reaction:

$$Ru^{III}(NPM\text{-}NO)\text{-}H_2O;\ H_2O + 1e^- = Ru^{II}(NPM\text{-}NO)\text{-}H_2O;\ H_2O$$
$$E_0 = 0.43V$$

while reaction

$$Ru^{III}(NPM\text{-}NO, NO) + 1e^- = Ru^{II}(NPM\text{-}NO, NO)$$
$$E_0 = 0.44V$$

also has similar potential but no pH dependence.

Overall, this study presents significant body of data indicating that previously reported peroxide product $[Ru^{IV}{-}OO]^{2+}$ is most likely a mixture of Ru complexes with single and doubly oxidized NPM ligand. This interpretation is consistent with EPR, RR and mass spectrometry characteristics of the product.

4.5. Implications for the Mechanism of Water Oxidation. *4.5.1. Role of Proximal Base in Water Oxidation.* Here we investigated the role of the proximal base on O−O bond formation. Computationally we have shown a TS of 0.38 eV in the presence of a proximal base. Multiple DFT calculations have reported significantly higher activation barriers for the reaction of $Ru^{V}{=}O$ with water in the absence of proximal base, with values ranging between 0.57 and 1.1 eV.[53,58−62]

DOI: 10.1021/jacs.6b08409
J. Am. Chem. Soc. 2016, 138, 15605−15616

We have also experimentally shown that the Ru^{IV}=O state demonstrates high facility in oxygen atom transfer, and thus, under similar experimental conditions, any close by non-coordinating nitrogen groups can be quickly modified to become N−O groups. This can likely explain interesting phenomena such as p-$[Ru(tpy)(pynap)H_2O]^{2+}$ complex being inactive in water oxidation while its d-$[Ru(tpy)(pynap)H_2O]^{2+}$ analogue is an active catalyst.[63] In p-$[Ru(tpy)(pynap)H_2O]^{2+}$, the noncoordinating nitrogen of the pynap ligand is located in close proximity to Ru center with a distance between Ru^{IV}=O···N (2.7 Å) (by DFT calculations, result is not shown), which is even closer than in NPM complex (2.9 Å). Thus, it likely undergoes ligand modification on a few seconds time scale; however, the p-$[Ru(tpy)(pynap)H_2O]^{2+}$ complex with modified pynap appears to be catalytically inactive. Oxygen atom transfer from the Ru^{IV}=O state can be potentially responsible for some spectroscopic observations by UV−vis which were misinterpreted. For instance, in $[Ru(tpy)(bpm)(H_2O)]^{2+}$ catalyst, where tpy =2,2′:6′,2″-terpyridine and bpm =2,2′-bipyrimidine, which contains two noncoordinating nitrogen ligands, rates of Ru^{V}=O formation and its reactivity with water were reported from UV−vis.[47,64] Reported changes in UV−vis in this system might be related to 2,2′-bipyrimidine modifications. Overall, our dynamic analysis has shown that noncoordinating nitrogen likely cannot be used in catalyst design as a proximal base. Other chemical bases should be explored and verified that they are not prone to modifications under catalytic conditions.

4.6. Significance of EPR Spectroscopy in Analysis of Water Oxidation Mechanisms. With our results presented here and prior publications,[37,41,42] we would like to advocate for use of EPR in analysis of catalytic water oxidation. Extensive reliance on UV−vis spectroscopy has been detrimental for the field of Ru-based homogeneous water oxidation. Note that the majority of Ru^{III}, Ru^{IV} and Ru^{V} species of Ru based catalysts absorb similarly and poorly in the visible range. As our current results and prior publications have shown claims of some kinetic mechanisms, the stability and the presence of particular intermediates based on UV−vis analysis were not later verified by more comprehensive spectroscopic techniques. In this particular study, the claimed instability of the $[Ru^{III}(NPM)(4\text{-}pic)_2(H_2O)]^{3+}$ and 50% content of $[Ru^{V}(NPM)(4\text{-}pic)_2{=}O]^{3+}$, based on UV−vis and electrochemical analysis, could not be verified. All Ru^{III} complexes are S = 1/2 which makes their EPR detection straightforward. g-tensors are highly specific and can indicate the presence of different species in complex mixtures. EPR is highly sensitive, and here it allowed detection of the small contribution of the Ru^{III} species with a modified ligand already in samples produced with 2 equiv of Ce^{IV}, while a larger content of this complex (produced with 4 equiv. and higher of Ce^{IV}) was required for RR detection.

4.7. Path of O−O Bond Formation. There is an accepted view in the field that Ru complexes form an O−O bond via nucleophilic attack of water on a highly oxidized Ru=O species. Currently, the major challenge in proving this hypothesis is the spectroscopic identification of the resulting peroxo or superoxo species. While several claims and proposals have been made in identifying the spectroscopic signatures of the peroxo species,[37,64,65] none so far have been firmly verified. Here we presented the reinterpretation of the reported peroxo species $[Ru^{IV}{-}OO]^{2+}$ to be a result of the oxidation of the noncoordinating nitrogen of the NPM ligand with formation of $[Ru^{III}(NPM\text{-}NO)(4\text{-}pic)_2H_2O]^{3+}$ and $[Ru^{III}(NPM\text{-}NO,NO)(4\text{-}pic)_2]^{3+}$. To the best of our knowledge, there is currently no solid proof of any detectable Ru based peroxide or superoxide species under catalytic conditions. This poses a significant challenge to the validity of the water nucleophilic attack hypothesis.

Similarly, the situation with monitoring the Ru^{V}=O species remains alarmingly unresolved. In the blue dimer catalyst, the Ru^{IV},Ru^{V} intermediate was confirmed; however, its product cannot be verified as a peroxide.[37] In single site catalysts with neutral polypyridine ligands, Ru^{V}=O species currently remain unverified in spite of their reported long lifetimes[47,64,66−71] while some complexes reaching the Ru^{V} state are reported to be inactive in O_2 evolution.[72,73]

The role of N−O groups as ligands to Ru in water oxidation is poorly understood. In $[Ru^{II}(NPM)(4\text{-}pic)_2(H_2O)]^{2+}$, NPM modification happens so quickly that it is not possible to delineate whether initial complex is a better or worse catalyst. Figure S12 compares the O_2 evolution of initial compound and sample after BE. It shows that prior ligand oxidation significantly decrease the lag phase in onset of water oxidation. Liu et al.[43] argued that the $[Ru(qpy)(L)_2]^{2+}$ series of catalysts are inactive unless qpy is converted to a qpy-N,N″-dioxide ligand. In the crystallized $[Ru(qpy\text{-}NO,NO)(L)_2]^{3+}$ complex, O−O distance is about ∼3.1 Å, and it was shown that the oxygens of N−O ligands do not exchange under catalytic condition, suggesting they are not actively involved with O−O bond formation.[43] In DFT models of $[Ru^{III}(NPM\text{-}NO,NO)]^{3+}$ and $[Ru^{IV}(NPM\text{-}NO,NO)]^{4+}$, oxygen atoms are much closer, at 2.6 and 2.4 Å, correspondingly. It appears that $[Ru^{III}(NPM\text{-}NO,NO)]^{3+}$ can evolve oxygen with small negative ΔG = −0.3 eV.

5. CONCLUSIONS

The single site Ru-based catalyst $Ru^{II}(NPM)(4\text{-}pic)_2(H_2O)]^{2+}$ was analyzed using a combination of EPR, millisecond−second freeze quench, X-ray absorption, and resonance Raman spectroscopic techniques. Experiments were supplemented with DFT calculations. Dynamics of oxygen atom transfer from Ru^{IV}=O to NPM ligand were uncovered. This facile reactivity likely prevents use of noncoordinating nitrogen as a base in WOC design. We expect other WOCs, including those with Fe and Co centers to show similar reactivity. New information on ligand modifications is essential, as these can activate as well as deactivate catalysts and thus should be understood and properly managed for development of future more active and durable catalysis.

■ ASSOCIATED CONTENT

Supporting Information

The Supporting Information is available free of charge on the ACS Publications website at DOI: 10.1021/jacs.6b08409.

EPR, EXAFS analysis, resonance Raman data, and DFT calculations (PDF)

■ AUTHOR INFORMATION

Corresponding Author

*ypushkar@purdue.edu

Notes

The authors declare no competing financial interest.

DOI: 10.1021/jacs.6b08409
J. Am. Chem. Soc. 2016, 138, 15605−15616

■ ACKNOWLEDGMENTS

This material is based upon work supported by the U.S. Department of Energy, Office of Sciences, Office of Basic Energy Sciences under Grant Numbers DE-FG02-10ER16184 (Y.P.), DE-FG02-07ER15888 (R.T. and R.Z.), and DE-AC02-06CH11357 (D.M.). R.T. and R.Z. also thank The Robert Welch Foundation (Grant E-621) for financial support. Use of the Advanced Photon Source, an Office of Science User Facility operated by the U.S. Department of Energy (DOE) Office of Science by Argonne National Laboratory, was supported by the U.S. DOE under Contract DE-AC02-06CH11357. PNC/XSD (Sector 20) facilities at the Advanced Photon Source, and research at these facilities, are supported by the US Department of Energy − Basic Energy Science, the Canadian Light Source and its funding partners, and the Advanced Photon Source. We thank Dr. Steve Heald and Dr. Dale Brewe for help with experiments at Beamline BM-20, APS. Dr. Polyansky is acknowledged for helpful discussions and supply of bulk electrolysis sample for EPR analysis. Access to EPR was provided by the Amy Instrumentation Facility, Department of Chemistry under the supervision of Dr. Michael Everly. We thank Dr. William Cramer and Dr. Stanislav Zakharov from structural biology at Purdue University for providing access to the SX20 Stopped-Flow UV−vis spectrometer (Applied Photophysics Ltd) and Dr. Yong Chen from the Department of Physics at Purdue University for allowing us to use the Xplora HORIBA Raman Microscope. M.P. is a NRC research associate.

■ REFERENCES

(1) Lewis, N. S.; Nocera, D. G. *Proc. Natl. Acad. Sci. U. S. A.* **2006**, *103*, 15729.
(2) Faunce, T. A.; Lubitz, W.; Rutherford, A. W.; MacFarlane, D.; Moore, G. F.; Yang, P. D.; Nocera, D. G.; Moore, T. A.; Gregory, D. H.; Fukuzumi, S.; Yoon, K. B.; Armstrong, F. A.; Wasielewski, M. R.; Styring, S. *Energy Environ. Sci.* **2013**, *6*, 695.
(3) Nocera, D. G. *Acc. Chem. Res.* **2012**, *45*, 767.
(4) Herrero, C.; Quaranta, A.; Leibl, W.; Rutherford, A. W.; Aukauloo, A. *Energy Environ. Sci.* **2011**, *4*, 2353.
(5) Blakemore, J. D.; Crabtree, R. H.; Brudvig, G. W. *Chem. Rev.* **2015**, *115*, 12974.
(6) House, R. L.; Iha, N. Y. M.; Coppo, R. L.; Alibabaei, L.; Sherman, B. D.; Kang, P.; Brennaman, M. K.; Hoertz, P. G.; Meyer, T. J. *J. Photochem. Photobiol., C* **2015**, *25*, 32.
(7) Wu, X. J.; Li, F.; Zhang, B. B.; Sun, L. C. *J. Photochem. Photobiol., C* **2015**, *25*, 71.
(8) Berardi, S.; Drouet, S.; Francas, L.; Gimbert-Surinach, C.; Guttentag, M.; Richmond, C.; Stoll, T.; Llobet, A. *Chem. Soc. Rev.* **2014**, *43*, 7501.
(9) Karkas, M. D.; Verho, O.; Johnston, E. V.; Akermark, B. *Chem. Rev.* **2014**, *114*, 11863.
(10) Kim, D.; Sakimoto, K. K.; Hong, D. C.; Yang, P. D. *Angew. Chem., Int. Ed.* **2015**, *54*, 3259.
(11) Swierk, J. R.; Mallouk, T. E. *Chem. Soc. Rev.* **2013**, *42*, 2357.
(12) Osterloh, F. E. *Chem. Soc. Rev.* **2013**, *42*, 2294.
(13) Singh, A.; Spiccia, L. *Coord. Chem. Rev.* **2013**, *257*, 2607.
(14) Gao, Y.; Ding, X.; Liu, J. H.; Wang, L.; Lu, Z. K.; Li, L.; Sun, L. C. *J. Am. Chem. Soc.* **2013**, *135*, 4219.
(15) Wickramasinghe, L. D.; Zhou, R. W.; Zong, R. F.; Vo, P.; Gagnon, K. J.; Thummel, R. P. *J. Am. Chem. Soc.* **2015**, *137*, 13260.
(16) Gersten, S. W.; Samuels, G. J.; Meyer, T. J. *J. Am. Chem. Soc.* **1982**, *104*, 4029.
(17) Wada, T. T. K.; Tsuge, K.; Tanaka, K. *Angew. Chem., Int. Ed.* **2000**, *39*, 1479.
(18) Deng, Z. P.; Tseng, H. W.; Zong, R. F.; Wang, D.; Thummel, R. *Inorg. Chem.* **2008**, *47*, 1835.
(19) Pramanik, N. C.; Bhattacharya, S. *Transition Met. Chem.* **1997**, *22*, 524.
(20) Yoshida, M.; Kondo, M.; Torii, S.; Sakai, K.; Masaoka, S. *Angew. Chem.* **2015**, *127*, 8092.
(21) Rabten, W.; Kärkäs, M. D.; Åkermark, T.; Chen, H.; Liao, R.; Tinnis, F.; Sun, J.; Siegbahn, P.; Andersson, P. G.; Åkermark, B. *Inorg. Chem.* **2015**, *54*, 4611.
(22) Zong, R.; Thummel, R. P. *J. Am. Chem. Soc.* **2005**, *127*, 12802.
(23) Concepcion, J. J.; Jurss, J. W.; Templeton, J. L.; Meyer, T. J. *J. Am. Chem. Soc.* **2008**, *130*, 16462.
(24) Kaveevivitchai, N.; Zong, R.; Tseng, H. W.; Chitta, R.; Thummel, R. P. *Inorg. Chem.* **2012**, *51*, 2930.
(25) Hirahara, M.; Ertem, M. Z.; Komi, M.; Yamazaki, H.; Cramer, C. J.; Yagi, M. *Inorg. Chem.* **2013**, *52*, 6354.
(26) Yagi, M.; Tajima, S.; Komi, M.; Yamazaki, H. *Dalton Trans.* **2011**, *40*, 3802.
(27) Honta, J.; Tajima, S.; Sato, T.; Saito, K.; Yui, T.; Yagi, M. *J. Photochem. Photobiol., A* **2015**, *313*, 126.
(28) Wrzolek, P.; Schwalbe, M. *Eur. J. Inorg. Chem.* **2015**, *2015*, 4373.
(29) Walden, A. G.; Miller, A. *Chem. Sci.* **2015**, *6*, 2405.
(30) Sheridan, M. V.; Sherman, B. D.; Fang, Z.; Wee, K.; Coggins, M. K.; Meyer, T. J. *ACS Catal.* **2015**, *5*, 4404.
(31) Polyansky, D. E.; Muckerman, J. T.; Rochford, J.; Zong, R.; Thummel, R. P.; Fujita, E. *J. Am. Chem. Soc.* **2011**, *133* (37), 14649.
(32) Yamazaki, H.; Hakamata, T.; Komi, M.; Yagi, M. *J. Am. Chem. Soc.* **2011**, *133*, 8846.
(33) Gao, Y.; Ding, X.; Liu, J. H.; Wang, L.; Lu, Z. K.; Li, L.; Sun, L. C. *J. Am. Chem. Soc.* **2013**, *135*, 4219.
(34) Duan, L. L.; Bozoglian, F.; Mandal, S.; Stewart, B.; Privalov, T.; Llobet, A.; Sun, L. C. *Nat. Chem.* **2012**, *4*, 418.
(35) Yamada, H.; Siems, W. F.; Koike, T.; Hurst, J. K. *J. Am. Chem. Soc.* **2004**, *126*, 9786.
(36) Cape, J. L.; Lymar, S. V.; Lightbody, T.; Hurst, J. K. *Inorg. Chem.* **2009**, *48*, 4400.
(37) Moonshiram, D.; Alperovich, I.; Concepcion, J. J.; Meyer, T. J.; Pushkar, Y. *Proc. Natl. Acad. Sci. U. S. A.* **2013**, *110*, 3765.
(38) Moonshiram, D.; Jurss, J. W.; Concepcion, J. J.; Zakharova, T.; Alperovich, I.; Meyer, T. J.; Pushkar, Y. *J. Am. Chem. Soc.* **2012**, *134*, 4625.
(39) Moonshiram, D.; Purohit, V.; Concepcion, J. J.; Meyer, T. J.; Pushkar, Y. *Materials* **2013**, *6*, 392.
(40) Alperovich, I.; Smolentsev, G.; Moonshiram, D.; Jurss, J. W.; Concepcion, J. J.; Meyer, T. J.; Soldatov, A.; Pushkar, Y. *J. Am. Chem. Soc.* **2011**, *133*, 15786.
(41) Pushkar, Y.; Moonshiram, D.; Purohit, V.; Yan, L.; Alperovich, I. *J. Am. Chem. Soc.* **2014**, *136*, 11938.
(42) Yan, L.; Zong, R.; Pushkar, Y. *J. Catal.* **2015**, *330*, 255.
(43) Liu, Y. Y.; Ng, S. M.; Yiu, S. M.; Lam, W. W. Y.; Wei, X. G.; Lau, K. C.; Lau, T. C. *Angew. Chem., Int. Ed.* **2014**, *53*, 14468.
(44) Matheu, R.; Ertem, M. Z.; Benet-Buchholz, J.; Coronado, E.; Batista, V. S.; Sala, X.; Llobet, A. *J. Am. Chem. Soc.* **2015**, *137*, 10786.
(45) Zong, R.; Thummel, R. P. *J. Am. Chem. Soc.* **2005**, *127*, 12802.
(46) Badiei, Y. M.; Polyansky, D. E.; Muckerman, J. T.; Szalda, D. J.; Haberdar, R.; Zong, R.; Thummel, R. P.; Fujita, E. *Inorg. Chem.* **2013**, *52*, 8845.
(47) Concepcion, J. J.; Jurss, J. W.; Norris, M. R.; Chen, Z. F.; Templeton, J. L.; Meyer, T. J. *Inorg. Chem.* **2010**, *49*, 1277.
(48) Ravel, B.; Newville, M. *J. Synchrotron Radiat.* **2005**, *12*, 537.
(49) Rehr, J. J.; Albers, R. C. *Rev. Mod. Phys.* **2000**, *72*, 621.
(50) Koningsberger, D. C.; Prins, R. *X Ray Absorption: Principles, Applications, Techniques of EXAFS, SEXAFS and XANES*; John Wiley & Sons: New York, 1988.
(51) Lachancegalang, K. J.; Doan, P. E.; Clarke, M. J.; Rao, U.; Yamano, A.; Hoffman, B. M. *J. Am. Chem. Soc.* **1995**, *117*, 3529.
(52) Lopez, I.; Ertem, M. Z.; Maji, S.; Benet-Buchholz, J.; Keidel, A.; Kuhlmann, U.; Hildebrandt, P.; Cramer, C. J.; Batista, V. S.; Llobet, A. *Angew. Chem., Int. Ed.* **2014**, *53*, 205.
(53) Hughes, T. F.; Friesner, R. A. *J. Phys. Chem. B* **2011**, *115*, 9280.
(54) Meyer, T. J.; Huynh, M. H. V. *Inorg. Chem.* **2003**, *42*, 8140.

DOI: 10.1021/jacs.6b08409
J. Am. Chem. Soc. 2016, 138, 15605−15616

(55) Wasylenko, D. J.; Ganesamoorthy, C.; Henderson, M. A.; Koivisto, B. D.; Osthoff, H. D.; Berlinguette, C. P. *J. Am. Chem. Soc.* **2010**, *132*, 16094.
(56) Wang, L.-P.; Wu, Q.; Van Voorhis, T. *Inorg. Chem.* **2010**, *49*, 4543.
(57) Masaoka, S.; Sakai, K. *Chem. Lett.* **2009**, *38*, 182.
(58) Vigara, L.; Ertem, M. Z.; Planas, N.; Bozoglian, F.; Leidel, N.; Dau, H.; Haumann, M.; Gagliardi, L.; Cramer, C. J.; Llobet, A. *Chem. Sci.* **2012**, *3*, 2576.
(59) Sala, X.; Ertem, M. Z.; Vigara, L.; Todorova, T. K.; Chen, W. Z.; Rocha, R. C.; Aquilante, F.; Cramer, C. J.; Gagliardi, L.; Llobet, A. *Angew. Chem., Int. Ed.* **2010**, *49*, 7745.
(60) Privalov, T.; Akermark, B.; Sun, L. C. *Chem. - Eur. J.* **2011**, *17*, 8313.
(61) Angeles-Boza, A. M.; Ertem, M. Z.; Sarma, R.; Ibanez, C. H.; Maji, S.; Llobet, A.; Cramer, C. J.; Roth, J. P. *Chem. Sci.* **2014**, *5*, 1141.
(62) Tong, L. P.; Inge, A. K.; Duan, L. L.; Wang, L.; Zou, X. D.; Sun, L. C. *Inorg. Chem.* **2013**, *52*, 2505.
(63) Boyer, J. L.; Polyansky, D. E.; Szalda, D. J.; Zong, R. F.; Thummel, R. P.; Fujita, E. *Angew. Chem., Int. Ed.* **2011**, *50*, 12600.
(64) Concepcion, J. J.; Jurss, J. W.; Norris, M. R.; Chen, Z. F.; Templeton, J. L.; Meyer, T. J. *Inorg. Chem.* **2010**, *49*, 1277.
(65) Stull, J. A.; Britt, R. D.; McHale, J. L.; Knorr, F. J.; Lymar, S. V.; Hurst, J. K. *J. Am. Chem. Soc.* **2012**, *134*, 19973.
(66) Chen, Z.; Concepcion, J. J.; Hull, J. F.; Hoertz, P. G.; Meyer, T. J. *Dalton Trans.* **2010**, *39*, 6950.
(67) Chen, Z. F.; Concepcion, J. J.; Hu, X. Q.; Yang, W. T.; Hoertz, P. G.; Meyer, T. J. *Proc. Natl. Acad. Sci. U. S. A.* **2010**, *107*, 7225.
(68) Chen, Z. F.; Concepcion, J. J.; Jurss, J. W.; Meyer, T. J. *J. Am. Chem. Soc.* **2009**, *131*, 15580.
(69) Concepcion, J. J.; Jurss, J. W.; Brennaman, M. K.; Hoertz, P. G.; Patrocinio, A. O. T.; Iha, N. Y. M.; Templeton, J. L.; Meyer, T. J. *Acc. Chem. Res.* **2009**, *42*, 1954.
(70) Concepcion, J. J.; Jurss, J. W.; Hoertz, P. G.; Meyer, T. J. *Angew. Chem., Int. Ed.* **2009**, *48*, 9473.
(71) Concepcion, J. J.; Jurss, J. W.; Templeton, J. L.; Meyer, T. J. *J. Am. Chem. Soc.* **2008**, *130*, 16462.
(72) Deng, Z. P.; Tseng, H. W.; Zong, R. F.; Wang, D.; Thummel, R. *Inorg. Chem.* **2008**, *47*, 1835.
(73) Tseng, H. W.; Zong, R.; Muckerman, J. T.; Thummel, R. *Inorg. Chem.* **2008**, *47*, 11763.

DOI: 10.1021/jacs.6b08409
J. Am. Chem. Soc. 2016, 138, 15605−15616